Nano Energy 68 (2020) 104334

Contents lists available at ScienceDirect

Nano Energy

journal homepage: http://www.elsevier.com/locate/nanoen

Communication

Two-photon-pumped high-quality, single-mode vertical cavity lasing based on perovskite monocrystalline films

Xiaohong Li [a], Weiwei Liu [a,*], Yiling Song [a], Hua Long [a], Kai Wang [a], Bing Wang [a], Peixiang Lu [a,b,**]

[a] Wuhan National Laboratory for Optoelectronics and School of Physics, Huazhong University of Science and Technology, Wuhan, 430074, China
[b] Laboratory of Optical Information Technology, Wuhan Institute of Technology, Wuhan, 430205, China

ARTICLE INFO

Keywords:
Hybrid perovskite
Monocrystalline film
Single-mode microlaser
Vertical-cavity surface-emitting laser
Integrated optoelectronic device

ABSTRACT

Single-mode microlasers are of crucial importance for high-performance integrated photonic devices. However, it still remains a significant challenge to achieve single-mode microlasers conveniently. In this work, we propose a strategy to realize high-quality, single-mode vertical-cavity surface-emitting lasers (VCSELs) based on hybrid perovskite monocrystalline films. Under two-photon pump, the VCSEL exhibits excellent performances with a remarkable low threshold of ~421 μJ/cm^2, a high quality factor (Q factor) of ~1286 and a small divergence angle of ~0.5°. Importantly, single-mode lasing with a good spatial coherence can be conveniently achieved with the VCSEL configuration, which significantly reduces the complexity for fabricating high-quality single-mode microlasers. In addition, switchable VCSEL can be realized by taking advantage of the anisotropic two-photon absorption of the hybrid perovskites. The single-mode vertical-cavity emission, excellent lasing performances, frequency up-conversion ability and switchable property will provide a versatile platform for high-performance nanosources and multifunctional integrated optoelectronic devices.

1. Introduction

In past years, hybrid perovskites have shown great promise for functional devices including solar cells [1–3], light-emitting devices [4,5] and field-effect transistors [6]. In particular, due to the high optical gain and broad tunability, hybrid perovskites have become excellent candidates for miniaturized lasing devices. For instance, perovskite nanowires and microplates would act as natural microcavities for Fabry-Pérot (F–P) and whispering-gallery-mode (WGM) lasers [7,8]. Besides, hybrid perovskites could be also engineered into various composite microcavity structures, such as microspheres [9,10], distributed-feedback cavities [11], photonic crystals [12] and dielectric arrays [13,14]. More recently, perovskites also gained considerable attention for realizing polariton lasing at room temperature [15]. Although previous studies have greatly promoted the development of high-performance perovskite microlasers, the multimode lasing output from most of the devices has seriously decreased the coherence and monochromaticity of the coherent nanosources. Typical methods to reduce the longitudinal modes in the optical cavity were expanding free spectral range with small cavity and filtering the cavity modes by coupled cavity structure [16–18]. However, the severe restrictions on the size and structure of the cavities would increase the inherent complexity in device configuration especially for high-quality single-crystal nanostructures, which imposed significant challenges for manufacturing of integrated microlasing devices. Therefore, developing a straightforward strategy to achieve a high-quality single-mode microlaser based on perovskites is essential.

In addition to the outstanding optoelectronic responses, hybrid perovskites have shown superior nonlinear optical properties, especially for nonlinear absorption and emission [19–24]. For examples, $CH_3NH_3PbBr_3$ ($MAPbBr_3$) perovskite crystals were reported to possess a strong two-photon absorption, which could be used for multifunctional nonlinear photodetectors [22]. 3D perovskite colloidal nanocrystals were revealed to exhibit a strong five-photon absorption, which enabled fresh approaches for next-generation multiphoton imaging [21]. Recently, 2D hybrid perovskites were demonstrated to have an

* Corresponding author.
** Corresponding author. Wuhan National Laboratory for Optoelectronics and School of Physics, Huazhong University of Science and Technology, Wuhan, 430074, China.
E-mail addresses: lwhust@hust.edu.cn (W. Liu), lupeixiang@hust.edu.cn (P. Lu).

https://doi.org/10.1016/j.nanoen.2019.104334
Received 20 September 2019; Received in revised form 23 November 2019; Accepted 26 November 2019
Available online 2 December 2019

extraordinary two-photon absorption, showing great potential for high-efficiency nonlinear emission [23,24]. Driven by the giant nonlinear responses, hybrid perovskites have become an ideal platform for multiphoton-pumped microlasers [25–29]. Moreover, the multiphoton-pumped regime has favorable advantages such as a large penetration depth and a small damage effect, which are critical for protecting the hybrid perovskite from degradation under high photon density [30].

In this work, we report a two-photon-pumped high-quality, single-mode vertical-cavity lasing based on $MAPbBr_3$ perovskite monocrystalline films. A vertical microcavity structure was fabricated by integrating large-area, high-quality $MAPbBr_3$ monocrystalline films with distributed Bragg reflector (DBR) and Ag mirrors. Under two-photon pump, exciton-polariton strong coupling can be observed, which will transit to the weak-coupling induced photonic lasing as the pump fluence increases. The vertical-cavity lasing possesses high performances with a low lasing threshold of ~421 μJ/cm^2, a high Q factor of ~1286, and a small far-field divergence of ~0.5°. Moreover, single-mode lasing with good spatial coherence can be conveniently achieved with the vertical-cavity configuration, which significantly reduces the complexity for fabricating high-quality single-mode microlasers. In addition, switchable lasing behavior can be demonstrated by tuning the pump polarization based on the anisotropic two-photon absorption of the $MAPbBr_3$ perovskite.

2. Results and discussion

$MAPbBr_3$ single crystals were synthesized using a well-established antisolvent-vapor-assisted crystallization growth (Supporting Information) [31]. In order to achieve large-area monocrystalline films, a pressure-induced spacing limitation was realized by clipping the precursor solution between two clean flat substrates, as schematically illustrated in Fig. 1(a). Fig. 1(b) shows an optical microscope image of an as-prepared $MAPbBr_3$ monocrystalline film on glass substrate. The $MAPbBr_3$ monocrystalline film has a lateral size over 600 μm. The smooth surface implies a good crystallinity of the $MAPbBr_3$ monocrystalline film. The height profile in Fig. 1(b) indicates that the thickness of the monocrystalline film is very uniform, with a concentrated distribution less than 8 μm (Fig. S1(b)). The X-ray diffraction (XRD) spectrum in Fig. 1(c) exhibits a dominant (*00h*) series of diffraction peaks, which corresponds to the cubic phase of $MAPbBr_3$ and agrees well with previous reports [31]. The monocrystalline film was further characterized by linear absorption and photoluminescence (PL) spectrum, as shown in Fig. 1(d). The absorption spectrum (black curve) exhibits a sharp absorption peak at ~522 nm (~2.38 eV), which is attributed to the excitonic absorption of $MAPbBr_3$. The PL spectrum (red curve) shows a sharp peak at ~547.6 nm (~2.26 eV) with a broad linewidth of ~22 nm, which are in good agreement with the literature reports [25,32].

For optical measurements, a femtosecond-pulsed Ti:sapphire regenerative amplifier centered at 800 nm was used as the light source. A 10 × microscope objective (NA = 0.25) was applied to focus the femtosecond laser beam onto the samples. Fig. 1(e) and (f) plot measured PL spectrum and the corresponding spectrally integrated PL intensity of the $MAPbBr_3$ monocrystalline film as a function of the pump power, respectively. Although oscillations appear in the PL spectra as the pump power increases, no amplified spontaneous emission (ASE) or lasing can be observed, implying that the optical feedback and gain are not strong enough to overcome the intrinsic loss in the $MAPbBr_3$ monocrystalline film. Fig. 1(f) shows that the integrated PL intensity has a quadratic dependence on the pump power, suggesting a two-photon pumped frequency-upconversion process.

DBR-based microcavities have been commonly used for microlasers and strong exciton-photon coupling, in which the photons can be strongly confined in the microcavity with a small mode volume [33–37]. Specifically, when the excited photons in the microcavity are near resonant with the interband exciton transition of the $MAPbBr_3$ perovskite, the photons will oscillate in the cavity and strongly interact with the excitons, thus forming the cavity polaritons, as illustrated in Fig. 2(a). In order to obtain an efficient optical feedback for a high gain, a microcavity structure was fabricated by embedding the $MAPbBr_3$ monocrystalline film between a DBR and a Ag mirror (Fig. S2, Supporting Information). Fig. 2(b) shows the cross-sectional scanning electron microscope (SEM) image of the fabricated microcavity

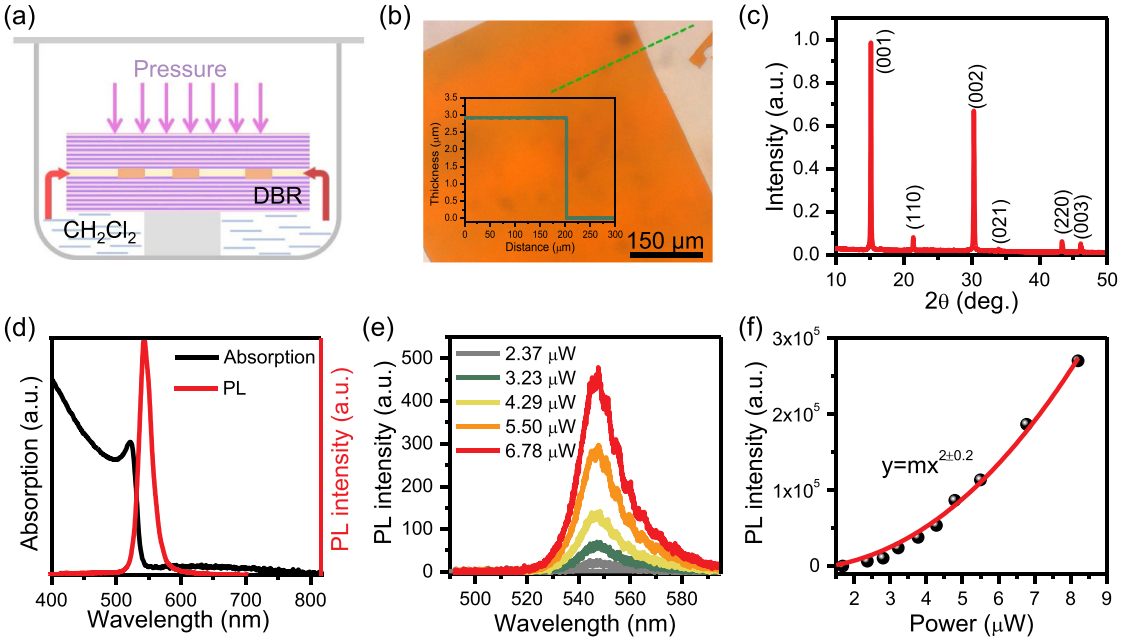

Fig. 1. (a) Schematic illustration for pressure-assisted growth of $MAPbBr_3$ monocrystalline films. (b) Optical microscope image and height profile of a $MAPbBr_3$ monocrystalline film on glass substrate. (c) XRD pattern of a $MAPbBr_3$ monocrystalline film. (d) Linear absorption and TPL spectra of the $MAPbBr_3$ monocrystalline film. (e) Two-photon-pumped PL (TPL) spectrum and (f) the corresponding spectrally integrated PL intensity of a $MAPbBr_3$ monocrystalline film as a function of the pump power, respectively.

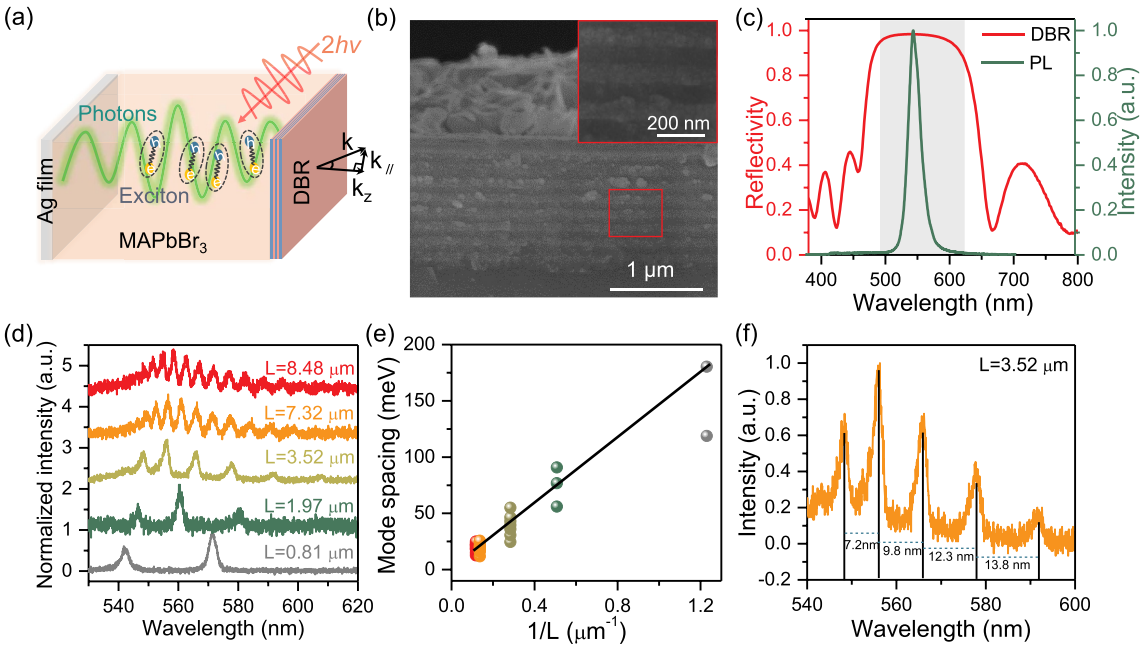

Fig. 2. (a) Schematic illustration for the exciton-photon interaction in the vertical cavity structure with $MAPbBr_3$ monocrystalline films. (b) Cross-sectional SEM image of the microcavity structure. The inset represents a zoomed-in image to show the optimized morphology of the SiO_2/TiO_2 layers. (c) Measured reflection spectrum of the DBR (red curve). The green curve represents the PL spectrum of $MAPbBr_3$. (d) Measured TPL spectra of the microcavity structures with various-thickness $MAPbBr_3$ monocrystalline films. (e) Plot of the mode spacing as a function of the inverse of the film thickness *L*. (f) A TPL spectrum for the microcavity structure with a 3.52-μm-thickness $MAPbBr_3$ monocrystalline film.

structure, in which the DBR multilayer stack structure can be clearly observed. In particular, the zoomed-in image in the inset of Fig. 2(b) displays smooth interfaces between the stack layers, indicating a high quality of the fabricated microcavity structure. Fig. 2(c) shows the measured reflection spectrum of the DBR facet of the microcavity structure (red curve). The DBR has a high reflection in the range from 490 nm to 620 nm with a maximum reflectivity over 98%, which can well cover the PL spectrum of $MAPbBr_3$ (green curve). Furthermore, the surface roughnesses of the DBR reflector, $MAPbBr_3$ monocrystalline film and the microcavity structure were quantitatively characterized. The root-mean-square (RMS) values of the surface roughness are 0.46 nm, 1.6 nm and 1.5 nm respectively (Fig. S3, Supporting Information), which demonstrate the smooth surface and high quality of the microcavity structure.

Fig. 2(d) presents the measured two-photon-absorption induced PL (TPL) spectra of the microcavity structures. The thickness of the $MAPbBr_3$ monocrystalline films varies from 0.81 μm to 8.48 μm. Notably, the oscillation in the PL spectra can be attributed to the cavity

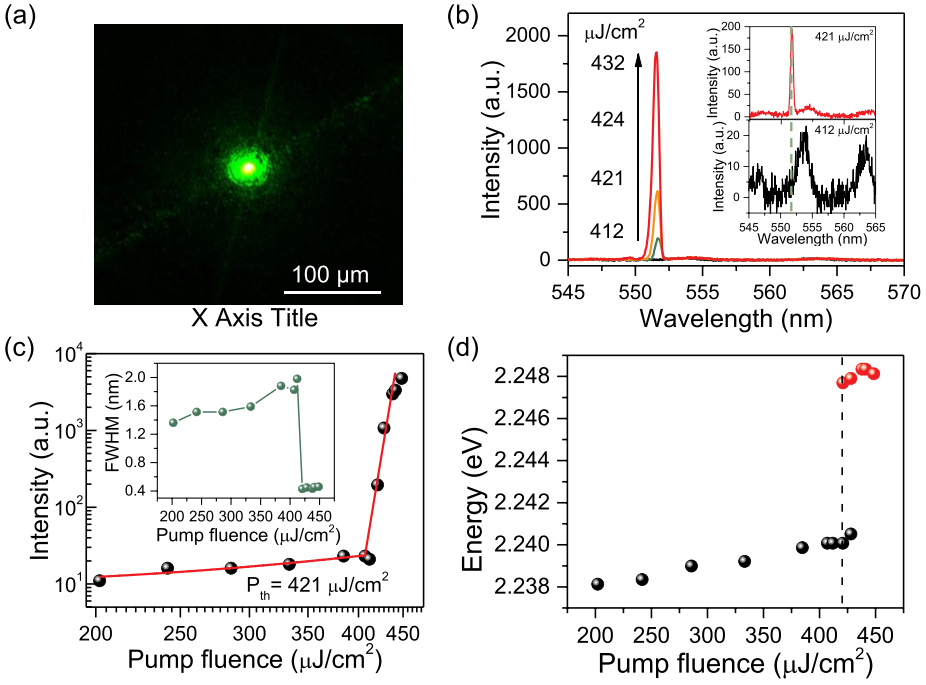

Fig. 3. (a) Dark-field image of the lasing emission from the microcavity structure. (b) TPL spectrum of the microcavity structure measured as a function of the pump fluence. Inset: enlarged plot of the TPL spectra below and above the lasing threshold (421 μJ/cm^2) respectively. (c) Log-log plot of PL peak intensity versus pump fluence. The inset presents a plot of the corresponding FWHM of the PL spectra versus the pump fluence. (d) Plot of the energy of polariton and photonic lasing modes versus the pump fluence.

modes. No uncoupled exciton spectrum is observed, indicating that the photonic modes can be strongly coupled with the perovskite excitons in the microcavity. Fig. 2(e) plots the mode spacing as a function of the inverse of the cavity length L (film thickness). The mode spacing is linear inversely to the cavity length, which is consistent with the F–P mode characteristics. Interestingly, a typical TPL spectrum for the microcavity structure (L = 3.52 μm) in Fig. 2(f) displays that with the increasing (decreasing) of wavelength (photon energy), the mode spacing between two adjacent modes gradually increases. The strong dispersion reveals an essential distinction from the normal photonic modes in the F–P cavity, which suggests the occurrence of exciton-photon strong coupling (details in Supporting Information) [32,38].

To investigate the lasing behavior of the $MAPbBr_3$ monocrystalline films in the microcavity structure, the active medium was pumped at higher intensity levels to overcome the optical loss. Fig. 3(a) shows a dark-field image of the light emitted outside from the surface of the microcavity with a pump fluence above the lasing threshold, in which a bright green spot can be observed. In particular, the spot displays a clear spatial interference patterns, indicating the generation of lasing emission with excellent coherence. For quantitative characterization, the TPL spectrum of the microcavity structure was measured versus the pump fluence, as shown in Fig. 3(b). At a low pump fluence, an oscillation spectrum dominated by the exciton-photon strong coupling is presented. As the pump fluence gradually increases, a sharp and narrow peak emerges between two adjacent polariton modes (inset of Fig. 3(b)). As the pump fluence is further increased, the intensity of the sharp peak experiences a rapid increase, demonstrating the occurrence of stimulated emission in the microcavity structure. Fig. 3(c) shows a log-log plot of the PL intensity as a function of the pump fluence. When the pump fluence is below 421 μJ/cm^2, the PL intensity increases slowly with the pump fluence. While as the pump fluence is above 421 μJ/cm^2, the PL intensity displays a superlinear increase. The typical "kink" characteristic in the log-log plot represents a typical feature for the transition from spontaneous emission to stimulated emission. Correspondingly, the two-photon pumped lasing threshold can be determined to be ~421 μJ/cm^2, which has been decreased by 5 times compared with that of the WGM lasing in the $MAPbBr_3$ microplates (Fig. S6, Supporting Information) [26]. Moreover, the inset of Fig. 3(c) shows that the FWHM of the PL spectra experiences a dramatic decrease above the lasing threshold, which suggests a sharp increase in the coherence and further demonstrates the lasing emission.

The variation feature of the FWHM can offer evidence to confirm the lasing mechanism. The inset of Fig. 3(c) shows that the FWHM is slightly broadened with the pump fluence below lasing threshold, due to the polariton-exciton interactions [15]. While beyond the lasing threshold, the FWHM broadening disappears and keeps nearly the same even though the pump fluence is further increased, which presents a typical feature for the normal photonic lasing. For confirmation, we monitored the variation of the photon energy corresponding to the emission peak as a function of pump fluence, as shown in Fig. 3(d). Below the lasing threshold, the photon energy shows a continuous blueshift with the pump fluence, demonstrating the polariton-exciton interaction process [39]. However, as the pump fluence increases above the lasing threshold, a new peak close to the cavity resonance appears suddenly in the PL spectrum, indicating that the lasing mode is distinct from the intrinsic polariton modes in the microcavity. The appearance of the new lasing mode is an evidence of the transition from the polariton-exciton strong coupling to the weak coupling regime, which is consistent with the variation feature of the FWHM [40]. Therefore, the physical mechanism for the lasing observed here can be attributed to the weak coupling induced photonic lasing, also well-known as the vertical-cavity surface-emitting laser (VCSEL).

Although several polariton modes exist in the PL spectrum below lasing threshold, only one photonic mode is amplified for lasing in the VCSEL with a 3.52-μm-thick $MAPbBr_3$ monocrystalline film. In principle, single-mode lasing will be realized when only one cavity mode is overlapped with the gain spectrum of the medium. Fig. 4(a) plots the amplified spontaneous emission (ASE) spectrum (black curve) of the $MAPbBr_3$ single crystal under two-photon pump. The ASE presents an optical amplified region between 545 nm and 557 nm, corresponding to a gain linewidth of ~6 nm around 552 nm. For the PL spectrum shown in Fig. 2(d), the adjacent mode spacing around the gain peak is ~7.4 nm, which is broader than the gain linewidth of the $MAPbBr_3$ single crystal. As a result, single-mode lasing can be produced with a 3.52-μm-thick $MAPbBr_3$ monocrystalline film. Based on the above analysis, we can estimate the ultimate thickness of the $MAPbBr_3$ monocrystalline film for single-mode VCSELs. For the laser spectra of F–P resonance, the adjacent mode spacing Δx can be expressed as [41].

$$\Delta x = \frac{\lambda^2}{2n_g L}, \tag{1}$$

where λ is the central wavelength of the adjacent modes, and L is the cavity length (film thickness). n_g represents the group refractive index of the lasing mode, which is dependent on the wavelength. The group refractive index around 552 nm is determined to be ~5.8 by fitting the relationship between $\lambda^2/2\Delta\lambda$ and L with a linear function (Fig. 4(b)), in which λ and Δx are extracted from the PL spectra for the microcavity structures with various-thickness $MAPbBr_3$ monocrystalline films. According to Equation (1), the ultimate thickness of the film thickness is calculated to be ~5.2 μm when only one mode is overlapped with the gain region (Δx = 6 nm). Experimental results in Fig. 4(c) shows that single-mode lasing can still be achieved with a 6.84-μm-thick $MAPbBr_3$ monocrystalline film. Although single-mode microlasers were obtained by selecting very small nanowires and microplates as the microcavity, the random distribution of the crystal sizes has prevented large-scale manufacturing of the desired devices [25,28]. In contrast, taking advantage of the pressure-assisted growth method, the thicknesses of the $MAPbBr_3$ monocrystalline films can be controlled to make sure that most (80%) of the samples are suitable for single-mode lasing (Fig. S1). Therefore, the integrated VCSEL configuration provides a convenient approach for manufacturing single-mode microlasers based on perovskite single crystals.

Quality factor (Q factor) and divergence angle are measured to characterize the performance of the single-mode VCSEL. Fig. 4(d) shows a typical lasing spectrum (black dots) and the fitted result with a Gaussian model (red curve). The FWHM of the lasing spectrum was fitted to be 0.43 nm, giving rise to a high Q factor of ~1286 ($Q = \lambda/\Delta\lambda$), and suggesting a high quality of the fabricated microcavity structure and $MAPbBr_3$ monocrystalline films. To determine the divergence angle of the VCSEL, the far-field pattern was measured using an angle-resolved Fourier imaging setup (Fig. S7, Supporting Information), as shown in Fig. 4(e) [15]. One can observe that the photons are dominantly distributed in the center of the far-field pattern, implying a small divergence of the laser beam. For quantitative determination, the intensity distribution along the crossline in Fig. 4(e) was extracted and presented in the inset (white dots). The experimental data can be well fitted with a Gaussian function, indicating the inherent Gaussian beam output from the VCSEL. Furthermore, the fitted result (red curve) shows that the laser beam has an angular divergence of ~0.5°, smaller than most of the best values reported for microlasers [16,42,43]. For the vertical cavity structure, the emissions can be strongly confined to oscillate along the longitudinal axis of the microcavity, resulting in a dominant vertical wavevector component [36,37]. Therefore, highly directional lasing emission can be obtained in the direction vertical to the microcavity surface. On the other hand, distinctly from the microcavity structures with subwavelength resonators [7,8], the planar microcavity cooperated with high-quality and large-area $MAPbBr_3$ monocrystalline films is advantageous for decreasing diffraction from the cavity facets, and preventing the beam from diverging in the far field. We also calculated the far-field angular divergence of a Gaussian beam emitted from the VCSEL microcavity by numerical simulation

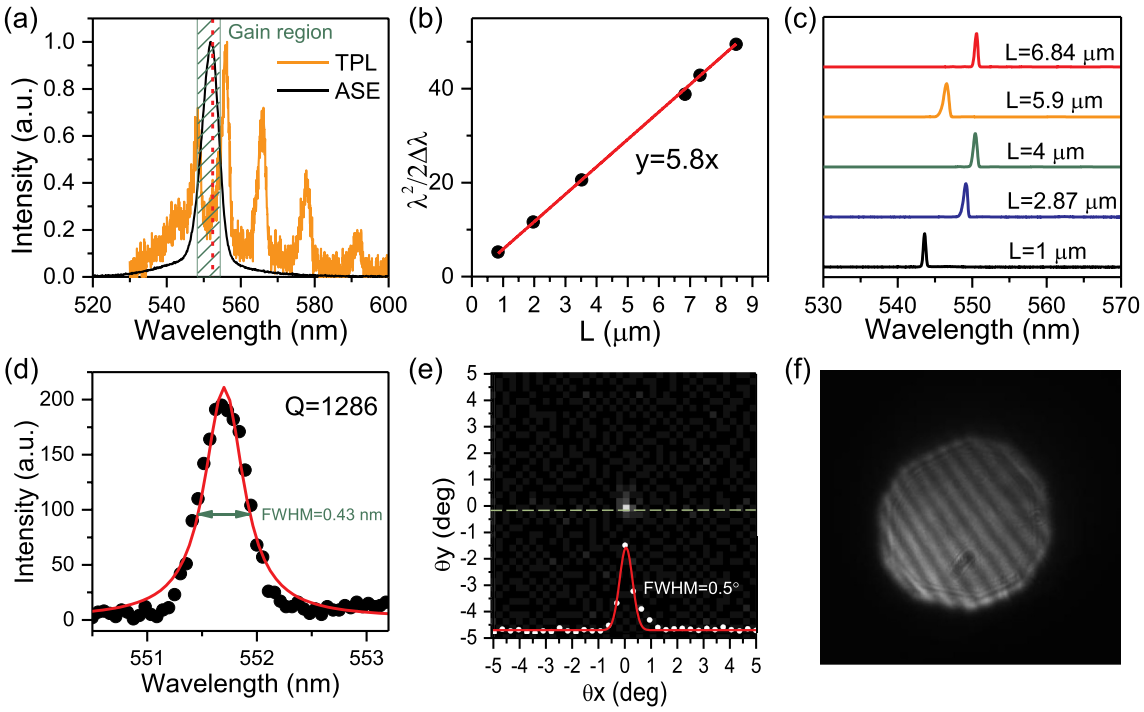

Fig. 4. (a) Plots of ASE spectrum of a $MAPbBr_3$ single crystal (black curve) and TPL spectrum of the microcavity structure (yellow curve). (b) Plot of the relationship between $\lambda^2/2\Delta\lambda$ and cavity length L. Red line represents the linear fitted result. (c) Measured lasing spectra for the VCSEL with various-thickness $MAPbBr_3$ monocrystalline films. (d) A typical lasing spectrum of the VCSEL (black dots), and the corresponding Gaussian fitted result (red curve). The FWHM of the lasing spectrum was fitted to be 0.43 nm. (e) Far-field pattern of the VCSEL measured with an angle-resolved Fourier imaging setup. Inset: the intensity distribution extracted along the crossline and the corresponding Gaussian fitting result. (f) Interference pattern between the two arms of the Michelson interferometer.

(Comsol Multiphysics), which agrees well with the experimental result (Fig. S8, Supporting Information). To further characterize the performance of the VCSEL, we checked the spatial coherence of the single-mode lasing emission with a Michelson interferometer. The interference pattern between the two arms of the interferometer was captured by a CCD camera, as displayed in Fig. 4(f) (Fig. S9, Supporting Information). Clear interference fringes can be identified in the image, which provides an exact evidence for the buildup of spatial coherence of the lasing emission. For comparison, Table 1 summarizes the typical parameters for two-photon pumped microlasers with different semiconductor nanostructures [26,27,44–48]. In general, the lasing performances (lasing threshold, Q factor, divergence angle and mode property) of our proposed VCSEL based on $MAPbBr_3$ monocrystalline films are superior to most of the others. Specifically, we present a single-mode lasing with very small divergence angle, which is ascribed to the unique and high-quality vertical microcavity structure.

$MAPbBr_3$ have a symmetrically cubic crystal morphology, thus leading to polarization dependent nonlinear properties. To investigate the anisotropy of the two-photon-pumped VCSEL, a half-wave plate was used to control the polarization of the pump laser. The angle between the polarization and the edge of the cubic crystal is defined as θ, as illustrated in Fig. 5(a). Fig. 5(b) presents the normalized TPL intensity of a $MAPbBr_3$ monocrystalline film as a function of angle θ, which displays a period of 90° and corresponds to the 4-fold rotational symmetry of the $MAPbBr_3$ crystal along the c-axis. Specifically, the maximums and minimums of the TPL intensity can be obtained when the laser polarization is parallel to the edges (θ = 0°, 90°, 180°, 270°) and diagonals (θ = 45°, 135°, 225°, 315°) of the cubic crystal respectively, due to the anisotropic two-photon absorption of the $MAPbBr_3$ crystal. As $MAPbBr_3$ has a space group of Pm3 m, the polarization-dependent TPL intensity can be expressed as [22].

$$I_{TPL} = A[1 + 2\sigma[\sin^4(\theta+\delta) - \sin^2(\theta+\delta)]]^2, \quad (2)$$

where A and δ are two fitted constants. σ is the anisotropic parameter. Fig. 5(b) shows that the experimental results can be well fitted by Equation (2), with σ being −0.14 (red curve). Then we measured the power-dependent PL of the microcavity structure at two specific polarization angles (θ = 0° and 45°) to investigate the influence of pump polarization on the lasing property. Fig. 5(c) shows that the lasing threshold at θ = 0° is approximately 528 μJ/cm^2, which is smaller than that at θ = 45° (~572 μJ/cm^2). For pump fluence between 528 μJ/cm^2 and 572 μJ/cm^2, lasing can be switched on and off by tuning the pump polarization from θ = 0° to θ = 45°, as shown in Fig. 5(d). The

Table 1
Summary of typical parameters for two-photon pumped microlasers with different semiconductor nanostructures.

Materials	Cavity architecture	Lasing threshold	Q factor	Divergence angle	Lasing mode	Ref.
$MAPbBr_3$ monocrystalline	vertical F–P cavity	421 μJ/cm^2	1286	0.5°	single mode	This work
$MAPbBr_3$ microwire	F–P cavity	674 μJ/cm^2	682	NA	multimode	[26]
$MAPbBr_3$ microdisk	WGM	2.2 mJ/cm^2	NA	NA	ASE	[25]
$CsPbBr_3$ microcube	F–P cavity	439 μJ/cm^2	1150	NA	multimode	[41]
$CsPbBr_3$ nanocrystals	WGM	900 μJ/cm^2	1700–3500	NA	multimode	[42]
$CsPbBr_3$:ZnO films	random lasing	569 μJ/cm^2	NA	NA	ASE	[43]
CdS microwire	F–P cavity	3.3 mJ/cm^2	1300	NA	multimode	[44]
CdSe/CdS heterostructures	WGM	1.5 mJ/cm^2	800	NA	single mode	[45]

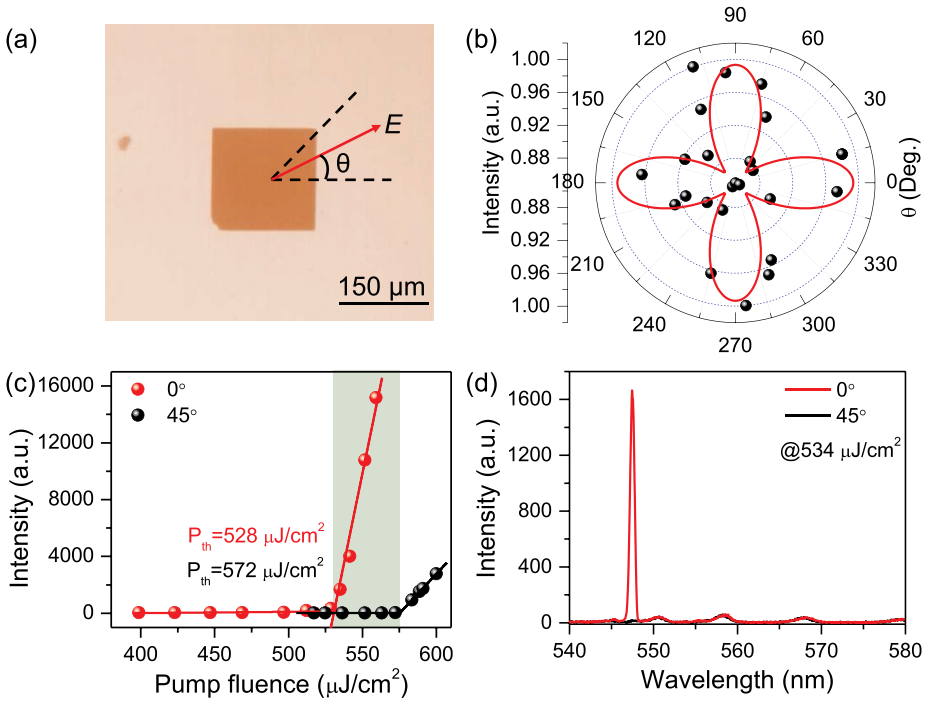

Fig. 5. (a) Schematic illustration for the angle θ between the polarization and the edge of the $MAPbBr_3$ monocrystalline film. (b) Plot of polarization-dependent TPL intensity of the $MAPbBr_3$ monocrystalline film. (c) Plots of integrated TPL intensity of the vertical microcavity structure versus the pump fluence, at $\theta^\circ = 0^\circ$ (red dots) and 45° (black dots) respectively. (d) Plots of TPL spectra measured at 534 μJ/cm^2, for $\theta^\circ = 0^\circ$ (red curve) and 45° (black curve) respectively.

polarization dependent property leads a new approach to controlling the lasing behavior, which shows great potential for functional applications such as optical switch and information encoding.

3. Conclusion

In summary, two-photon-pumped high-quality, single-mode VCSELs were realized based on $MAPbBr_3$ monocrystalline films. The VCSEL has a low lasing threshold of ~421 μJ/cm^2, which has been reduced by 5 times compared with the two-photon pumped WGM lasing. Moreover, single-mode lasing can be conveniently achieved with the VCSEL configuration, which significantly reduces the complexity for fabricating single-mode microlasers. The single-mode VCSEL exhibits excellent performances with a high Q factor of ~1286, a small divergence angle of ~0.5° and a good spatial coherence. In addition, switchable VCSEL has been demonstrated by taking advantage of the anisotropic two-photon absorption of the $MAPbBr_3$ perovskite. The single-mode vertical-cavity emission, excellent lasing performances, frequency up-conversion ability and switchable property suggest that the two-photon-pumped VCSELs show great promise for high-performance coherent nanosources and multifunctional integrated optoelectronic devices.

Declaration of interest statement

The authors declare no competing financial interests.

Acknowledgements

This work was supported by the National Natural Science Foundation of China (Nos. 11804109, 11204097 and 11674117). We acknowledge the Analytical & Testing Center of Huazhong University of Science and Technology (HUST) for XRD measurements, and the Center of Micro-Fabrication and Characterization (CMFC) of WNLO for the support in step profiler measurements.

Appendix A. Supplementary data

Supplementary data to this article can be found online at https://doi.org/10.1016/j.nanoen.2019.104334.

References

[1] Q. Jiang, Y. Zhao, X. Zhang, X. Yang, Y. Chen, Z. Chu, Q. Ye, X. Li, Z. Yin, J. You, Surface passivation of perovskite film for efficient solar cells, Nat. Photonics 13 (2019) 460.
[2] J.P. Correa-Baena, M. Saliba, T. Buonassisi, M. Gratzel, A. Abate, W. Tress, A. Hagfeldt, Promises and challenges of perovskite solar cells, Science 358 (2017) 739.
[3] Y. Wang, M. Li, X. Zhou, P. Li, X. Hu, Y. Song, High efficient perovskite whispering-gallery solar cells, Nano Energy 51 (2018) 556.
[4] K.B. Lin, J. Xing, L.N. Quan, F.P.G. de Arquer, X.W. Gong, J.X. Lu, L.Q. Xie, W. J. Zhao, D. Zhang, C.Z. Yan, W.Q. Li, X.Y. Liu, Y. Lu, J. Kirman, E.H. Sargent, Q. H. Xiong, Z.H. Wei, Perovskite light-emitting diodes with external quantum efficiency exceeding 20 per cent, Nature 562 (2018) 245.
[5] Y.F. Miao, Y. Ke, N.N. Wang, W. Zou, M.M. Xu, Y. Cao, Y. Sun, R. Yang, Y. Wang, Y. F. Tong, W.J. Xu, L.D. Zhang, R.Z. Li, J. Li, H.P. He, Y.Z. Jin, F. Gao, W. Huang, J. P. Wang, Stable and bright formamidinium-based perovskite light-emitting diodes with high energy conversion efficiency, Nat. Commun. 10 (2019) 3624.
[6] S.P. Senanayak, B.Y. Yang, T.H. Thomas, N. Giesbrecht, W.C. Huang, E. Gann, B. Nair, K. Goedel, S. Guha, X. Moya, C.R. McNeill, P. Docampo, A. Sadhanala, R. H. Friend, H. Sirringhaus, Understanding charge transport in lead iodide perovskite thin-film field-effect transistors, Sci. Adv. 3 (2017), e1601935.
[7] H.M. Zhu, Y.P. Fu, F. Meng, X.X. Wu, Z.Z. Gong, Q. Ding, M.V. Gustafsson, M. T. Trinh, S. Jin, X.Y. Zhu, Lead halide perovskite nanowire lasers with low lasing thresholds and high quality factors, Nat. Mater. 14 (2015) 636.
[8] Q. Zhang, R. Su, X. Liu, J. Xing, T.C. Sum, Q. Xiong, High-quality whispering-gallery-mode lasing from cesium lead halide perovskite nanoplatelets, Adv. Funct. Mater. 26 (2016) 6238.
[9] B.R. Sutherland, S. Hoogland, M.M. Adachi, C.T.O. Wong, E.H. Sargent, Conformal organohalide perovskites enable lasing on spherical resonators, ACS Nano 8 (2014) 10947.
[10] X.S. Tang, Z.P. Hu, W.W. Chen, X. Xing, Z.G. Zang, W. Hu, J. Qiu, J. Du, Y.X. Leng, X.F. Jiang, L.Q. Mai, Room temperature single-photon emission and lasing for all-inorganic colloidal perovskite quantum dots, Nano Energy 28 (2016) 462.
[11] M. Saliba, S.M. Wood, J.B. Patel, P.K. Nayak, J. Huang, J.A. Alexander-Webber, B. Wenger, S.D. Stranks, M.T. Horantner, J.T.W. Wang, R.J. Nicholas, L.M. Herz, M.B. Johnston, S.M. Morris, H.J. Snaith, M.K. Riede, Structured organic-inorganic perovskite toward a distributed feedback laser, Adv. Mater. 28 (2016) 923.

[12] S. Chen, K. Roh, J. Lee, W.K. Chong, Y. Lu, N. Mathews, T.C. Sum, A. Nurmikko, A photonic crystal laser from solution based organo-lead iodide perovskite thin films, ACS Nano 10 (2016) 3959.
[13] A. Zhizhchenko, S. Syubaev, A. Berestennikov, A.V. Yulin, A. Porfirev, A. Pushkarev, I. Shishkin, K. Golokhvast, A.A. Bogdanov, A.A. Zakhidov, A. A. Kuchmizhak, Y.S. Kivshar, S.V. Makarov, Single-mode lasing from imprinted halide-perovskite microdisks, ACS Nano 13 (2019) 4140.
[14] N. Zhang, W. Sun, S.P. Rodrigues, K. Wang, Z. Gu, S. Wang, W. Cai, S. Xiao, Q. Song, Highly reproducible organometallic halide perovskite microdevices based on top-down lithography, Adv. Mater. 29 (2017) 1606205.
[15] R. Su, C. Diederichs, J. Wang, T.C.H. Liew, J. Zhao, S. Liu, W. Xu, Z. Chen, Q. Xiong, Room-temperature polariton lasing in all-inorganic perovskite nanoplatelets, Nano Lett. 17 (2017) 3982.
[16] S.T. Chen, C. Zhang, J. Lee, J. Han, A. Nurmikko, High-Q, low-threshold monolithic perovskite thin-film vertical-cavity lasers, Adv. Mater. 29 (2017) 1604781.
[17] J. Zhao, Y. Yan, C. Wei, W. Zhang, Z. Gao, Y.S. Zhao, Switchable single-mode perovskite microlasers modulated by responsive organic microdisks, Nano Lett. 18 (2018) 1241.
[18] H. Hodaei, M.A. Miri, M. Heinrich, D.N. Christodoulides, M. Khajavikhan, Parity-time-symmetric microring lasers, Science 346 (2014) 975.
[19] T. Yamada, Y. Yamada, Y. Nakaike, A. Wakamiya, Y. Kanemitsu, Photon emission and reabsorption processes in $CH_3NH_3PbBr_3$ single crystals revealed by time-resolved two-photon-excitation photoluminescence microscopy, Phys. Rev. Appl. 7 (2017), 014001.
[20] F.O. Saouma, C.C. Stoumpos, J. Wong, M.G. Kanatzidis, J.I. Jang, Selective enhancement of optical nonlinearity in two-dimensional organic-inorganic lead iodide perovskites, Nat. Commun. 8 (2017) 742.
[21] W. Chen, S. Bhaumik, S.A. Veldhuis, G. Xing, Q. Xu, M. Gratzel, S. Mhaisalkar, N. Mathews, T.C. Sum, Giant five-photon absorption from multidimensional core-shell halide perovskite colloidal nanocrystals, Nat. Commun. 8 (2017) 15198.
[22] G. Walters, B.R. Sutherland, S. Hoogland, D. Shi, R. Comin, D.P. Sellan, O.M. Bakr, E.H. Sargent, Two-photon absorption in organometallic bromide perovskites, ACS Nano 9 (2015) 9340.
[23] W. Liu, J. Xing, J. Zhao, X. Wen, K. Wang, P. Lu, Q. Xiong, Giant two-photon absorption and its saturation in 2D organic-inorganic perovskite, Adv. Opt. Mater. 5 (2017) 1601045.
[24] W. Liu, X. Li, Y. Song, C. Zhang, X. Han, H. Long, B. Wang, K. Wang, P. Lu, Cooperative enhancement of two-photon-absorption-induced photoluminescence from a 2D perovskite-microsphere hybrid dielectric structure, Adv. Funct. Mater. 28 (2018) 1707550.
[25] W. Zhang, L. Peng, J. Liu, A. Tang, J.-S. Hu, J. Yao, Y.S. Zhao, Controlling the cavity structures of two-photon-pumped perovskite microlasers, Adv. Mater. 28 (2016) 4040.
[26] B. Yang, X. Mao, S. Yang, Y. Li, Y. Wang, M. Wang, W.-Q. Deng, K.-L. Han, Low threshold two-photon-pumped amplified spontaneous emission in $CH_3NH_3PbBr_3$ microdisks, ACS Appl. Mater. Interfaces 8 (2016) 19587.
[27] Z.Y. Gu, K.Y. Wang, W.Z. Sun, J.K. Li, S. Liu, Q.H. Song, S.M. Xiao, Two-photon pumped CH3NH3PbBr3 perovskite microwire lasers, Adv. Opt. Mater. 4 (2016) 472.
[28] Z.Z. Liu, J. Yang, J. Du, Z.P. Hu, T.C. Shi, Z.Y. Zhang, Y.Q. Liu, X.S. Tang, Y. X. Leng, R.X. Li, Robust subwavelength single-mode perovskite nanocuboid laser, ACS Nano 12 (2018) 5923.
[29] M. Li, M. Zhi, H. Zhu, W.-Y. Wu, Q.-H. Xu, M.H. Jhon, Y. Chan, Ultralow-threshold multiphoton-pumped lasing from colloidal nanoplatelets in solution, Nat. Commun. 6 (2015) 8513.
[30] H.H. Fang, S. Adjokatse, H.T. Wei, J. Yang, G.R. Blake, J.S. Huang, J. Even, M. A. Loi, Ultrahigh sensitivity of methylammonium lead tribromide perovskite single crystals to environmental gases, Sci. Adv. 2 (2016), e1600534.
[31] Q. Liao, K. Hu, H.H. Zhang, X.D. Wang, J.N. Yao, H.B. Fu, Perovskite microdisk microlasers self-assembled from solution, Adv. Mater. 27 (2015) 3405.
[32] S. Zhang, Q.Y. Shang, W.N. Du, J. Shi, Z.Y. Wu, Y. Mi, J. Chen, F.J. Liu, Y.Z. Li, M. Liu, Q. Zhang, X.F. Liu, Strong exciton-photon coupling in hybrid inorganic-organic perovskite micro/nanowires, Adv. Opt. Mater. 6 (2018) 1701032.
[33] J. Kasprzak, M. Richard, S. Kundermann, A. Baas, P. Jeambrun, J.M.J. Keeling, F. M. Marchetti, M.H. Szymanska, R. Andre, J.L. Staehli, V. Savona, P.B. Littlewood, B. Deveaud, L.S. Dang, Bose-Einstein condensation of exciton polaritons, Nature 443 (2006) 409.
[34] K.S. Daskalakis, S.A. Maier, R. Murray, S. Kena-Cohen, Nonlinear interactions in an organic polariton condensate, Nat. Mater. 13 (2014) 272.
[35] X. Liu, T. Galfsky, Z. Sun, F. Xia, E.-c. Lin, Y.-H. Lee, S. Kéna-Cohen, V.M. Menon, Strong light–matter coupling in two-dimensional atomic crystals, Nat. Photonics 9 (2015) 30.
[36] Y. Liu, W. Yang, S. Xiao, N. Zhang, Y. Fan, G. Qu, Q. Song, Surface-emitting perovskite random lasers for speckle-free imaging, ACS Nano 13 (2019) 10653.
[37] Y. Wang, X.M. Li, V. Nalla, H.B. Zeng, H.D. Sun, Solution-processed low threshold vertical cavity surface emitting lasers from all-inorganic perovskite nanocrystals, Adv. Funct. Mater. 27 (2017) 1605088.
[38] T. Tawara, H. Gotoh, T. Akasaka, N. Kobayashi, T. Saitoh, Cavity polaritons in InGaN microcavities at room temperature, Phys. Rev. Lett. 92 (2004) 256402.
[39] N. Peyghambarian, H.M. Gibbs, J.L. Jewell, A. Antonetti, A. Migus, D. Hulin, A. Mysyrowicz, Blue shift of the exciton resonance due to exciton-exciton interactions in a multiple-quantum-well structure, Phys. Rev. Lett. 53 (1984) 2433.
[40] S. Kim, B. Zhang, Z.R. Wang, J. Fischer, S. Brodbeck, M. Kamp, C. Schneider, S. Hofling, H. Deng, Coherent polariton laser, Phys. Rev. X 6 (2016) 011026.
[41] M.T. Hill, M.C. Gather, Advances in small lasers, Nat. Photonics 8 (2014) 908.
[42] A.K. Yang, T.B. Hoang, M. Dridi, C. Deeb, M.H. Mikkelsen, G.C. Schatz, T. W. Odom, Real-time tunable lasing from plasmonic nanocavity arrays, Nat. Commun. 6 (2015) 6939.
[43] S. Noda, Photonic crystal lasers-ultimate nanolasers and broad-area coherent lasers, J. Opt. Soc. Am. B 27 (2010) B1.
[44] Z. Hu, Z. Liu, Y. Bian, D. Liu, X. Tang, W. Hu, Z. Zang, M. Zhou, L. Sun, J. Tang, Y. Li, J. Du, Y. Leng, Robust cesium lead halide perovskite microcubes for frequency upconversion lasing, Adv. Opt. Mater. 5 (2017) 1700419.
[45] Y.Q. Xu, Q. Chen, C.F. Zhang, R. Wang, H. Wu, X.Y. Zhang, G.C. Xing, W.W. Yu, X. Y. Wang, Y. Zhang, M. Xiao, Two-photon-pumped perovskite semiconductor nanocrystal lasers, J. Am. Chem. Soc. 138 (2016) 3761.
[46] C. Li, Z. Zang, C. Han, Z. Hu, X. Tang, J. Du, Y. Leng, K. Sun, Highly compact CsPbBr3 perovskite thin films decorated by ZnO nanoparticles for enhanced random lasing, Nano Energy 40 (2017) 195.
[47] L. Zhang, K. Wang, Z. Liu, G. Yang, G. Shen, P. Lu, Two-photon pumped lasing in a single CdS microwire, Appl. Phys. Lett. 102 (2013) 211915.
[48] G.C. Xing, Y.L. Liao, X.Y. Wu, S. Chakrabortty, X.F. Liu, E.K.L. Yeow, Y. Chan, T. C. Stun, Ultralow-threshold two-photon pumped amplified spontaneous emission and lasing from seeded CdSe/CdS nanorod heterostructures, ACS Nano 6 (2012) 10835.

Xiaohong Li is currently pursuing her Ph. D. at Wuhan National Laboratory for Optoelectronics (WNLO), Huazhong University of Science and Technology (HUST), China. Her research interest focuses on the nanolasing devices based on hybrid perovskites.

Weiwei Liu received his B. S. and Ph.D. degrees in optical engineering and electronics from HUST, in 2012 and 2017 respectively. During his doctoral research, he visited for exchange in Nanyang Technological University, Singapore, in 2015. In 2017, he joined the School of Physics at HUST. His research interests have been focused on nonlinear optics and nanophotonics.

Yiling Song received her B. S. at Central South University, China, in 2016. She is currently pursuing her Ph. D. in optics at HUST. Her research interests include nonlinear optical properties and functional devices based on nanostructures.

Hua Long received her B. S., M. S., and Ph. D. degrees from HUST, in 1999, 2002, and 2008 respectively. She is currently an associate professor in the School of Physics, HUST. Her research interests include surface plasmonics, metasurfaces, and ultrafast spectra.

Kai Wang received his B. S. and Ph. D. degrees in physical electronics at HUST, in 2006 and 2011 respectively. He is currently a professor in the School of Physics, HUST. His recent research interest focuses on nonlinear optics, metasurfaces, and ultrafast spectra.

Bing Wang received the B. S. and Ph. D. degrees in physics from Wuhan University, China, in 2002 and 2007 respectively. He worked as a postdoctoral researcher in National Scientific Research Center (NSRC), France, from 2007 to 2009, and then as a research fellow in the Agency for Science, Technology, and Research (A*STAR), Singapore. In 2013, he joined the School of Physics at HUST, as a full professor. His current research interests have been focused on nanophotonics and topological photonics.

Peixiang Lu received his B.S. degree in physics from Peking University, China, in 1987, and then received the Ph. D. degree from Shanghai Institute of Optics and Fine Mechanics (SIOM), the Chinese Academy of Sciences (CAS) in 1992. He has been worked as a research fellow in SIOM, Max Planck Institute (Germany), and NTT basic Research Laboratories (Japan), from 1992 to 2003. In 2003, he joined as a full professor in HUST. His research interests include ultrafast optics, attosecond physics and nanophotonics. He was elected as the OSA fellow in 2015.